

## Article

# Mechanical Properties and Damage Constitutive Model of Thermally Damaged Basalt

Wenzhao Chen <sup>1</sup>, Rui Chang <sup>1</sup> , Xiqi Liu <sup>2,3,\*</sup>, Yan Chang <sup>2,3</sup>, Fuqing Zhang <sup>4</sup>, Dongwei Li <sup>5</sup> and Zhenhua Wang <sup>4</sup>

<sup>1</sup> School of Civil Engineering, University of South China, Hengyang 421001, China; chengwz@usc.edu.cn (W.C.); cr452485907@163.com (R.C.)

<sup>2</sup> Pearl River Water Resources Research Institute, Guangzhou 510611, China; 13573366805@163.com

<sup>3</sup> Research Center on Pearl River Estuary & Coast, Ministry of Water Resources, Guangzhou 510611, China

<sup>4</sup> School of Civil and Architecture Engineering, East China University of Technology, Nanchang 330013, China; 19956818577@163.com (F.Z.); yingqinghua102@sina.com (Z.W.)

<sup>5</sup> College of Civil Engineering and Architecture, Dalian University, Dalian 116622, China; msz1981877712@163.com

\* Correspondence: liuxx142857@163.com

**Abstract:** Nuclear power is a high-quality clean energy source, but nuclear waste is generated during operation. The waste continuously releases heat during disposal, increasing the adjoining rock temperature and affecting the safety of the disposal site. Basalt is widely considered a commonly used rock type in the repository. This study of basalt's mechanical characteristics and damage evolution after thermal damage, with its far-reaching engineering value, was conducted by combining experimental work and theory. Uniaxial compression tests were conducted on basalt exposed to 25 °C, 500 °C, 700 °C, 900 °C, and 1100 °C conditions, and acoustic emission (AE) equipment was utilized to observe the acoustic emission phenomenon during deformation. This study was carried out to examine the mechanical characteristics, the sound emission features, the progression of damage laws, and the stress–strain framework of basalt after exposure to different types of thermal harm. As the temperature rises, the rock's maximum strength declines steadily, the peak strain rises in tandem, the rock sample's ductility is augmented, the failure mode changes from shear to tensile failure, and cracks in the failure area are observed. At room temperature, the acoustic emission signal is more vigorous than in the initial stage of rock sample loading due to thermal damage; however, after the linear elastic stage is entered, its activity is lessened. In cases where the rock approaches collapse, there is a significant surge in acoustic emission activity, leading to the peak frequency of acoustic emission ringing. The cumulative ring count of acoustic emission serves as the basis for the definition of the damage variable. At room temperature, the damage evolution of rock samples can be broken down into four distinct stages. This defined damage variable is more reflective of the entire failure process. After exposure to high temperatures, the initial damage of the rock sample becomes more extensive, and the damage variable tends to be stable with strain evolution. The stress–strain constitutive model of basalt deformation is derived based on the crack axial strain law and acoustic emission parameters. A powerful relationship between theoretical and experimental curves is evident.

**Keywords:** thermal damage; basalt; uniaxial compression; acoustic emission; damage evolution; constitutive model



**Citation:** Chen, W.; Chang, R.; Liu, X.; Chang, Y.; Zhang, F.; Li, D.; Wang, Z. Mechanical Properties and Damage Constitutive Model of Thermally Damaged Basalt. *Sustainability* **2024**, *16*, 3570. <https://doi.org/10.3390/su16093570>

Academic Editors: Barry D. Solomon and Changhyun Roh

Received: 26 January 2024

Revised: 21 April 2024

Accepted: 22 April 2024

Published: 24 April 2024



**Copyright:** © 2024 by the authors. Licensee MDPI, Basel, Switzerland. This article is an open access article distributed under the terms and conditions of the Creative Commons Attribution (CC BY) license (<https://creativecommons.org/licenses/by/4.0/>).

## 1. Introduction

As the base-bearing source of the “zero carbon” energy system, the nuclear power industry urgently needs to meet the significant strategic needs of the country's “double carbon” target [1]. The World Nuclear Energy Alliance is devoted to augmenting the utilization of nuclear energy and other low-carbon technologies to meet carbon reduction objectives [2], with nuclear energy being a potential answer to global climate change. The

rapid advancement of nuclear energy has enabled the establishment of a green, low-carbon economy, guaranteeing sustainable energy growth and providing immense benefits to humanity; however, it has also caused an upsurge in the amount of nuclear waste [3].

For nuclear waste disposal and deep rock mass engineering construction, frequently, it is essential to take into account the impact of elevated temperatures on rocks [4–7]. The engineering significance of studying the mechanical features and the law of destruction development in rock after thermal harm is thus considerable.

Much research has been conducted by scholars both domestically and abroad on the mechanical properties of rocks after thermal damage. Yan-jun Shen et al. [8] examined how cracks spread in high-temperature granite when exposed to various cooling shocks and obtained the temperature range for crack macro-morphology mutation through experiments and numerical simulation. Tubing Yin et al. [9] employed a servo-regulated compressor alongside an acoustic emission (AE) surveillance system and investigated how temperature and varying load conditions affect the elastic properties of standard rocks, discovering a notably higher sensitivity of the elasticity to temperature changes compared to strain. Zhao et al. [10] investigated how Beishan granite, when thermally impaired, conducts heat under uniaxial compression through the transient plane source (TPS) technique. The heat treatment temperature's augmentation caused the cumulative acoustic emission hit amount at the crack damage stress and peak stress to rise non-linearly, the sample's initial thermal conductivity and peak thermal conductivity diminished, and their divergence was augmented. Zhi Cheng Tang et al. [11] investigated the physical, thermal, and mechanical characteristics of fine-textured marble and discovered that heat treatment weakened the rock's properties while increasing its ductility during deformation, despite varying temperatures (20, 200, 300, 400, 500, and 600 °C) and time spans (0.5, 1, 2, 3, 4, and 8 h). When the treatment temperature reached 300 °C, the high-temperature duration had less impact on the rock's properties than did the temperature magnitude during treatment. By combining scanning electron microscopy (SEM) techniques, P.K. Gautam et al. [12] investigated the thermal effects on the physical and mechanical properties of Jalore granite in India. The findings revealed that the rock's compressive and tensile strength grew gradually with a temperature decrease below 300 °C, but plummeted sharply above 300 °C. Based on the Lemaitre strain equivalence theory, Zhu Zhennan et al. [13] assumed that the strength of thermally damaged rock micro-units obeyed a normal distribution, and the micro-unit failure conformed to the Mohr–Coulomb strength criterion. A variable for thermal damage was incorporated, followed by the creation of a statistical model for the constitutive thermal damage of rock post-high-temperature establishment. Liu et al. [14] adopted the Drucker–Prager criterion and Weibull distribution to establish a statistical damage constitutive model of high-temperature granite considering the damage threshold, residual stress, and thermal damage. Yaoliang Zhu et al. [15] proposed a rock fatigue damage model considering the influence of temperature based on phenomenology. Fatigue damage is defined using the residual strain method, and the Harris attenuation function is introduced to characterize the evolution of cyclic damage. The proposed model takes into account the influence of initial damage and temperature. Wang et al. [16] studied the tensile strength, Young's modulus, Poisson's ratio, and thermal expansion coefficient of granite at 1000 °C, and deduced the temperature dependence, taking into account the influence of initial damage and temperature in the proposed model. The uniaxial compression test was used to validate the novel constitutive law, which was integrated with the traditional Mohr–Coulomb model's strain softening and tension cut-off. Wang et al. [17] analyzed the three-shear Drucker–Prager yield criterion: a compaction coefficient, damage variable correction factor, and thermal damage variable were introduced. A novel comprehensive thermo-mechanical constitutive model was developed, taking into account the rock's compaction phase in the uniaxial compression test and its strain-softening due to thermal shock. After exposure to high temperatures, the model can accurately portray the entire rock damage process with strain alteration.

The previously mentioned academics carried out organized investigations into the mechanical characteristics of rocks post-high-temperature exposure, deriving numerous significant insights by integrating different tools and techniques. Nonetheless, the studies primarily concentrated on the examination of mechanical aspects, with lesser emphasis on the law governing the evolution of rock damage. Three primary approaches exist for analyzing rock damage and the constitutive model: (1) the definition of the damage variable and the determination of its correlation with stress and strain were derived from experimental results. (2) This relationship between the damage variable and stress and strain is established by the random distribution of the strength of the rock micro-element, and three primary approaches exist to analyze rock damage and the constitutive model. (3) The damage tensor is established using the homogenization theory to study the failure law of rock. However, in the case of rock subjected to elevated temperatures, only a handful of academics have examined its damage and constitutive model through the analysis of acoustic emission parameters. The intricate composition of basalt minerals, along with their varying thermal expansion coefficients, leads to thermal stress between them when exposed to high temperatures, thus causing cracks to form within the rock [18,19]. Acoustic emission technology can be used to monitor the change in microcracks in rock in real time [20]. Consequently, a more profound comprehension of basalt's failure process post-thermal damage is essential to more accurately determine the link between acoustic emission parameters and alterations in basalt's mechanical characteristics and failure mechanisms. In this study, uniaxial compression tests were carried out on basalt after different temperature treatments, and the results were studied in conjunction with acoustic emission parameters. The findings of this study are anticipated to serve as a crucial guide in the fields of nuclear waste management and the construction of deep rock mass engineering.

## 2. Test Scheme and Test Process

### 2.1. Rock Sample Selection and Heating Process

The basalt selected in the experiment was taken from Wutai County, Shanxi Province, and the rock samples had good integrity. Pyroxene and plagioclase were the main minerals of their composition, with olivine, hornblende, biotite, apatite, and other secondary minerals also present. The longitudinal wave velocity of the samples ranged from 5801.71 to 6015.02 m/s, and the density ranged from 2.896 g/cm<sup>3</sup> to 2.916 g/cm<sup>3</sup>, with relatively small dispersion. The International Society of Rock Mechanics [21] prescribed the transformation of the sample into a cylindrical form, measuring 50 mm in diameter and 100 mm in length. To guarantee uniformity in the characteristics of the samples, all the samples were taken from the same basalt; these are shown in Figure 1. Fifteen rock specimens were chosen and divided into three groups, each containing five rock specimens, to conduct five sets of uniaxial acoustic emission tests at room temperature (25 °C) and various temperatures (500 °C, 700 °C, 900 °C, and 1100 °C). A KSL-1200X muffle furnace (Sino-US joint venture Hefei Kejing Materials Technology Co., Ltd., Hefei, China) served as the heating device. At a rate of 20 °C/min, the specimens were heated and kept at that temperature for an hour before being placed in a furnace to reach room temperature.

### 2.2. Test Equipment and Method

#### (1) Uniaxial loading

The loading equipment adopted the MTS 815 high-rigidity rock mechanics test system, as shown in Figure 2. The hydraulic servo-control system is a system that can display real-time test curves and automatically record and store data. The axial loading capacity reaches a peak of 4600 kN, and the rigidity of the testing system is  $11.0 \times 10^9$  N/m. The experiment implemented deformation control, maintaining a loading speed of 0.05 mm/min until the sample was ultimately disposed of.



**Figure 1.** Basalt samples.

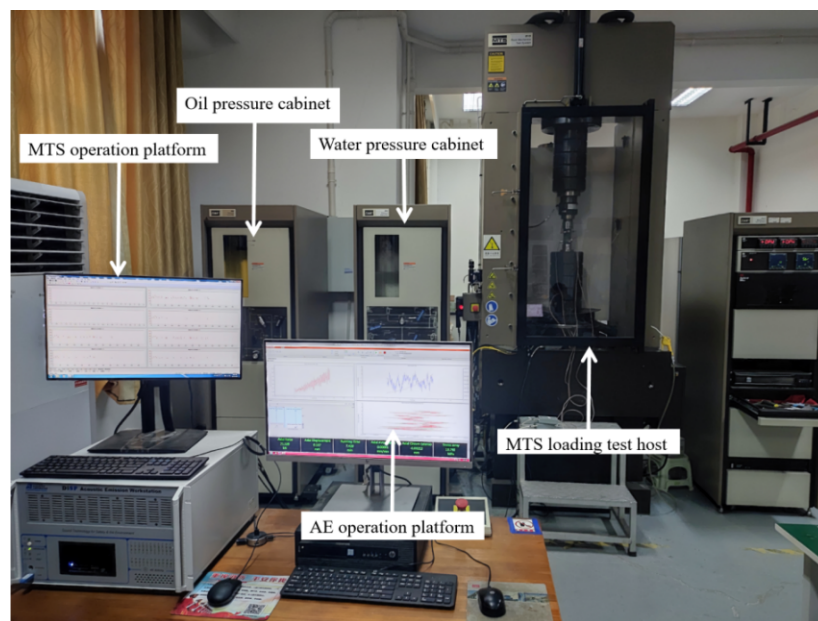


**Figure 2.** Test apparatus.

## (2) Acoustic emission monitoring

The system for monitoring acoustic emissions employed the American Physics Acoustic Corporation's (PAC) PCI-II acoustic emission testing system. Figure 3 shows a threshold of 45 dB, with a pre-gain of 45 dB, a sampling frequency of 1 MHz, and the RT50-AE acoustic emission sensor (American Physical Acoustics Company Beijing Representative Office, Beijing, China). Vaseline was used as a bridge between the acoustic emission probe and the rock sample to reduce signal weakening. At the start of the compression examination, acoustic emissions were monitored and data were gathered.



**Figure 3.** Acoustic emission monitoring system.

### 3. Mechanical Properties of Thermally Damaged Basalt

#### 3.1. The Apparent Morphology and Failure Mode of Basalt after High-Temperature Exposure

When basalt is subjected to high temperatures, it induces chemical changes in the mineral composition of the rock sample, leading to a transformation in its observable structure. Figure 4 displays the morphology of a rock sample after various temperature treatments.



**Figure 4.** Basalt apparent morphology.

It can be seen from Figure 4 that the rock sample was lead gray at room temperature. When the heat treatment temperature reached 500 °C, the apparent morphology of the rock sample was a flaxen color. When the temperature reached 700 °C, the apparent morphology of the rock sample was a beige color. When the temperature reached 900 °C, the apparent morphology of the rock sample was a soil color. When the rock sample reached 1100 °C, it took on a purple–black form, characterized by significant volumetric expansion and the appearance of cracks.

Figure 5 illustrates how basalt fails due to thermal damage. Our observations indicate variations in the failure patterns of the rock samples following exposure to diverse temperatures. At room temperature, the rock sample showed shear failure, mainly due to the shear stress on the fracture surface exceeding its shear strength, and the crack mode was mainly an inverted Y-shaped crack. At a temperature of 500 °C, the rock specimen displayed shear failure, causing the fracture surface to shift towards the center. This caused the fracture surface to appear at the top and the secondary crack to be in the middle. Additionally, many small cracks were present around the primary shear cracks. The rock sample at 700 °C also showed shear failure. At 900 °C, the rock sample underwent a transition from shear failure to tensile failure, with a Y-shaped fracture and primary and secondary cracks that were staggered. This fracture section had a variety of cracks, with the primary ones usually parallel. The rock sample at 1100 °C showed tensile failure. Radial tensile stress surpassing the rock's tensile strength was the primary cause, and the fracture surface was parallel or nearly parallel to the loading direction.

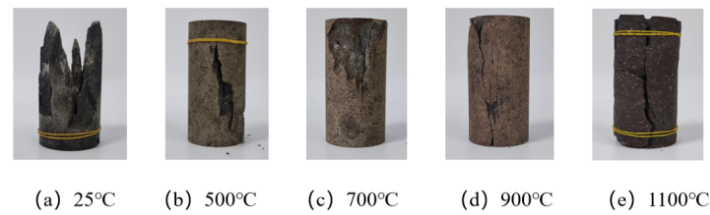


**Figure 5.** Thermal damage failure modes of basalt.

As the experimental temperature increased, the basalt underwent thermal damage, causing changes in its structure, microcrack development, and mineral composition. When the minerals reached a certain critical temperature, they underwent a phase shift, resulting in diminished particle bonding and subsequent deterioration of the rock. The varying types of rock materials caused varying levels of deterioration in the same rock sample's bearing segments, resulting in a variety of material strengths. As axial stress increased on the rock specimen, the weaker parts initially gave way, resulting in a decrease in bearing capacity and, in turn, the transfer of stress. At 700 °C, the rock samples underwent peak stress of 170.54 MPa, which then rose to 127.63 MPa after 900 °C. This stress and elastic strain in the rigid region caused shear cracks to expand and fuse, leading to shear failure in the uniaxial compression test. With the maximum stress of the rock sample being significantly reduced post-900 °C compared to 700 °C, it is deduced that the pivotal temperature for basalt minerals' phase change is between 700 °C and 900 °C, resulting in a transition from shear to tensile failure after 900 °C. In Figure 5c, it can be seen that the basalt was destroyed after exposure to 700 °C: it did not have fully penetrated shear cracks and had many small splitting cracks resulting from the combined action of tensile cracks and shear cracks.

### 3.2. Mechanical Properties of Basalt under Different Temperatures

Figure 6 displays the mean values of the test data for each set of rock samples. As the physical and mechanical properties of rock samples differ at different temperatures, the peak strengths closest to the average were selected for this study. Figure 7 displays the uniaxial compressive stress–strain curve of basalt under various temperatures. The results suggest that the uniaxial compressive stress–strain dynamics of rock specimens exposed to different temperatures can be divided into five stages, each corresponding to one of the five stages of gradual rock failure: crack closure, elasticity, stability of crack propagation, unsteadiness of crack propagation, and post-peak failure.

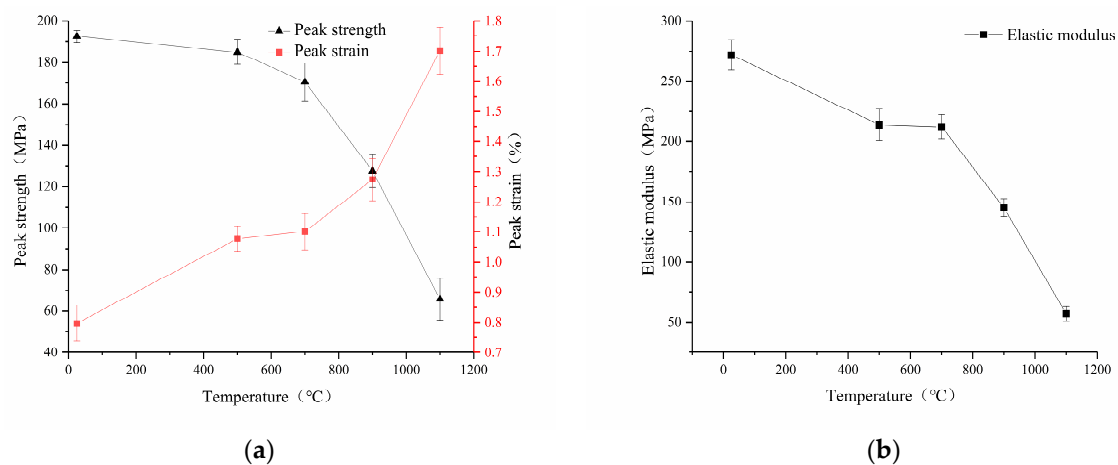


**Figure 6.** The physical and mechanical parameters of basalt after exposure to different temperatures. (a) The peak strength and peak strain. (b) The elastic modulus.

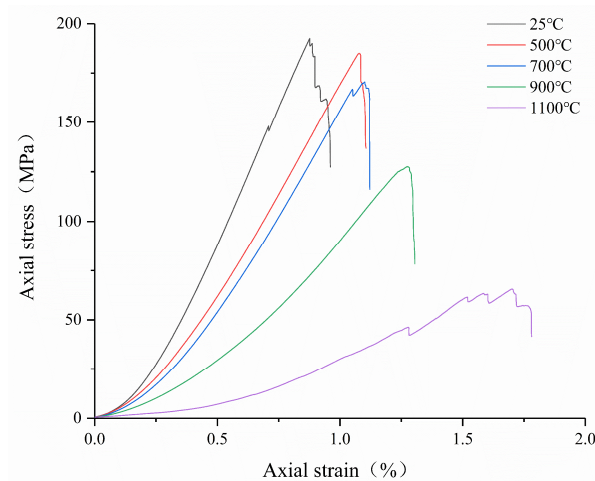


**Figure 7.** The uniaxial compressive stress–strain curves of basalt after exposure to different temperatures.

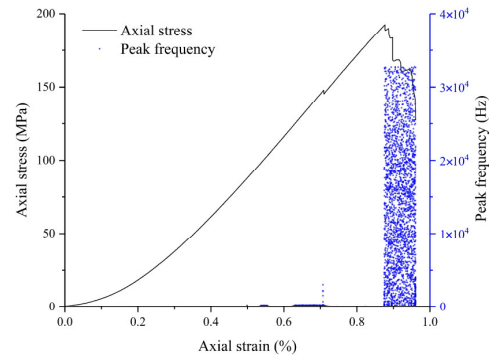
The five stages above are, respectively, reflected in Figure 7. During the phase of crack sealing, there is a steady rise in the curve's gradient, and as the temperature escalates, so does the duration of the crack-sealing phase, signifying that higher temperatures lead to increased initial thermal harm in the rock specimen and a higher count of microcracks within it. During the elastic phase, the curve's gradient remains steady and progressively diminishes as the temperature rises. No discernible decline in the curve's incline is observed before 1100 °C, indicating that the rock sample has no discernible plastic yield capability. After 1100 °C, a plastic region with an irregular association between strain and stress appears, and a yield platform is then formed. When the stress continues to increase, the rock sample undergoes fracture failure. At the same time, a noteworthy decrease in tension and a considerable rise in strain is seen, culminating in a distinct peak that symbolizes the peak of the curve. In the post-peak failure stage, before 900 °C, the stress sharply decreases, the strain remains unchanged, and the curve decreases almost linearly, showing brittle failure. However, the curve at 1100 °C has a stress fluctuation phenomenon, showing obvious plastic characteristics.

The rock specimens experienced peak stress levels of 192.56, 185.04, 170.54, 127.63, and 65.64 MPa at temperatures of 25 °C, 500 °C, 700 °C, 900 °C, and 1100 °C, in that order. As the temperature increased, the maximum stress experienced by the specimens decreased in proportion. The decrease amplitudes at 500 °C and 700 °C were almost the same. Nonetheless, the maximum stress experienced by the rock samples exposed to 900 °C decreased to 66.3% compared to those at ambient temperature (25 °C), suggesting that temperatures between 700 °C and 900 °C lead to more significant thermal harm to the rock samples. The thermal expansion of particles within a rock can vary, resulting in structural thermal stress that can cause either formation of new cracks or enlargement of existing ones. This leads to a deterioration of the mechanical properties of basalt and a decrease in its strength. At temperatures ranging from 700 °C to 900 °C, minerals undergo phase transformation, thus decreasing their bearing capacity [22]; in other words, some minerals start to decompose, resulting in a gradual decline of basalt's mechanical properties. When the temperature reaches about 1100 °C, the basalt undergoes intense melting, and the crystal state of the rock worsens. Furthermore, the rock sample loses its bearing capacity. As strength decreases, the stress–strain curve's compaction phase lengthens, the elastic phase contracts, and the peak stress-associated maximum strain increases. This is due to the high temperature improving the rock's ductility. Moreover, a rise in temperature causes a decrease in the elastic modulus of basalt.

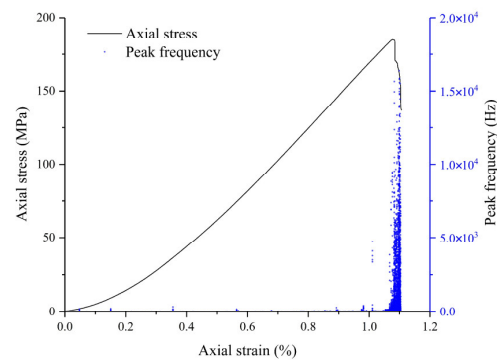
## 4. Acoustic Emission Characteristics of Thermally Damaged Basalt

### 4.1. Acoustic Emission Peak Frequency

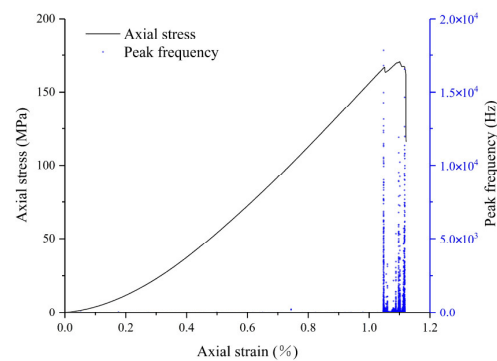
The characteristics of acoustic emissions in the frequency domain align with the data available on the scale of rock fractures [23]. Microcracks, known for their swift expansion and confined scope, are capable of producing sound emission signals at higher peak frequencies, while those at lower frequencies correlate with the formation of microcracks that propagate more slowly and in a high-frequency manner. The varying acoustic emission frequencies of basalt specimens may be the source of the intrinsic fracture principle. Figure 8 displays the peak frequency of basalt acoustic emission at various temperatures.



(a)

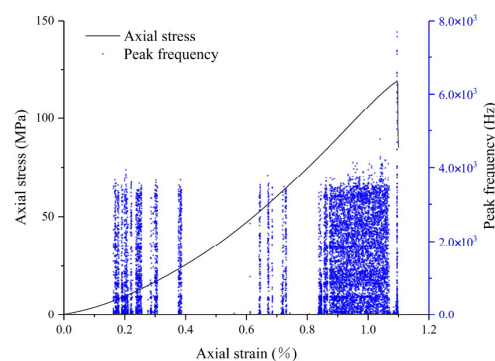


(b)

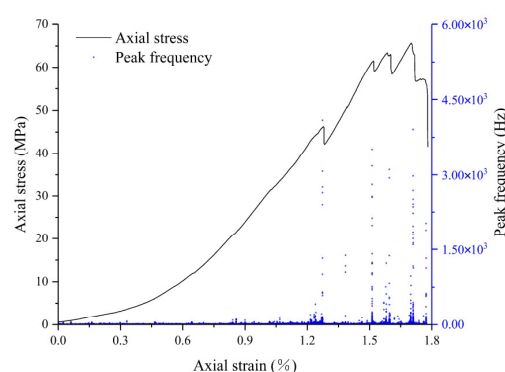


(c)

Figure 8. Cont.



(d)



(e)

**Figure 8.** The stress–strain curves of basalt and the corresponding acoustic emission peak frequencies after different temperatures are changed. (a) 25 °C. (b) 500 °C. (c) 700 °C. (d) 900 °C. (e) 1100 °C.

Figure 8 shows that before 900 °C, there are only very few acoustic emission signals during the initial loading phase, attributed to the reduced number of primary fractures in basalt specimens, and the peak frequency aggregation occurs near the peak stress. Post-900 °C, a heightened peak frequency appeared before reaching peak stress, attributed to the modified manner in which rocks fail due to damage caused by heat. There is an increase in the peak frequency preceding the maximum stress level of the rock specimen. The rock's fluctuating collapse due to elevated temperatures results in a decrease in peak frequency from its peak to its lowest at the point of elastic energy release, leading to a rebalancing of the fracture surface's stress state amidst this unstable failure. The healing of cracks and the further growth of local ones take place in the course of the procedure. As the temperature increases, the peak frequency aggregation time advances, and the duration becomes longer, but the maximum peak frequency decreases. Studies show that fissures caused by thermal damage accelerate the early development of small cracks, accelerating their expansion but reducing their total spread.

#### 4.2. Acoustic Emission Ringing Count

The count of signal oscillations whose amplitude surpasses a certain threshold is referred to as 'acoustic emission ringing count'. The frequency of ringing per time unit is indicative of the rate of acoustic emission ringing, while the aggregate number of ringing in each phase is equal to the total acoustic emission ringing. The frequency of ringing mirrors both the overall and individual activities of the rock's sound emission, aligning closely with the formation, enlargement, merging, and infiltration of fissures in the rock. The rate and total count of acoustic emission ringing were selected for this research study's

analytical purposes. Figure 9 displays the stress–strain curves of the rock samples under varying temperatures, along with the change law of acoustic emission parameters.

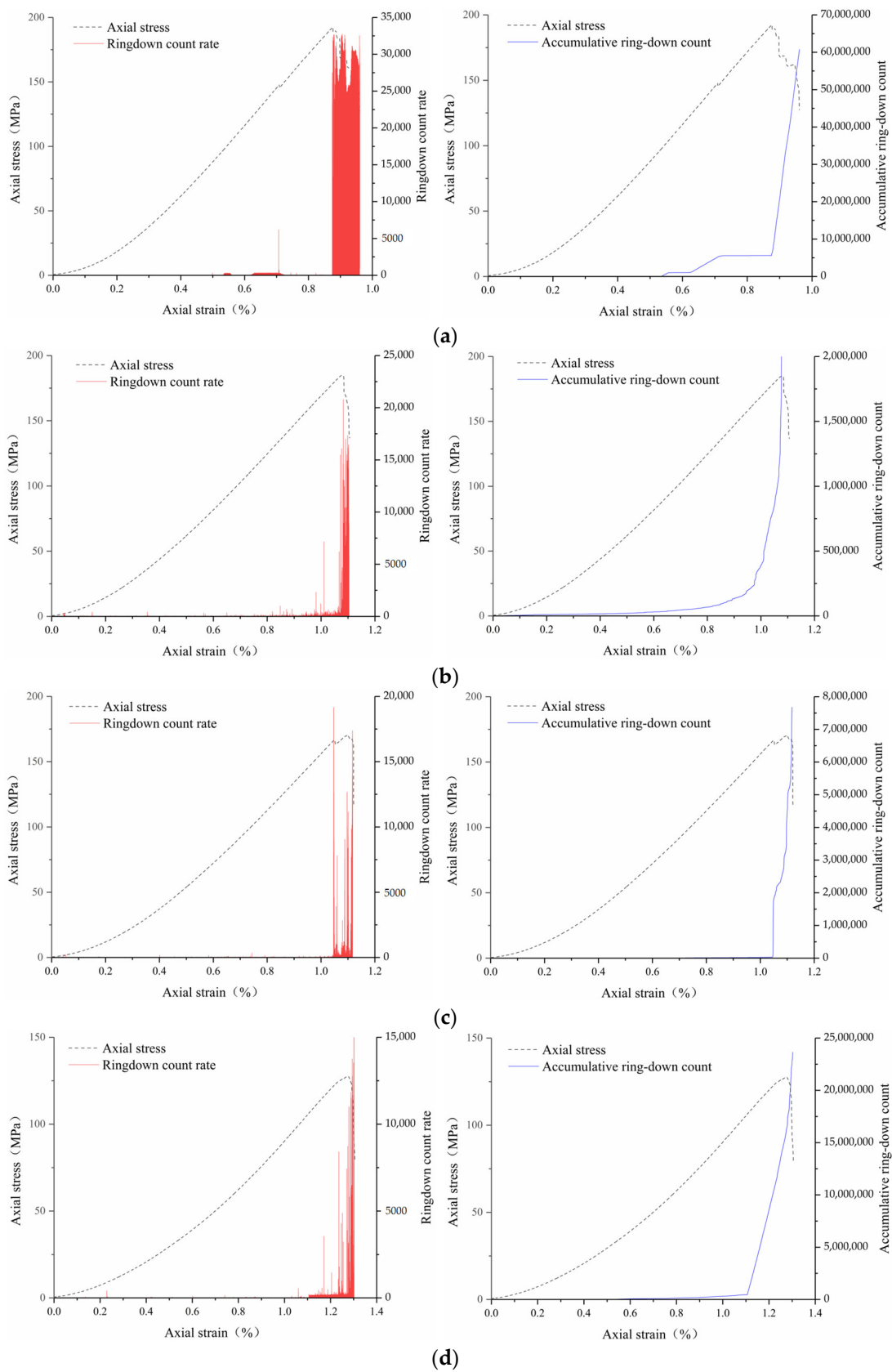
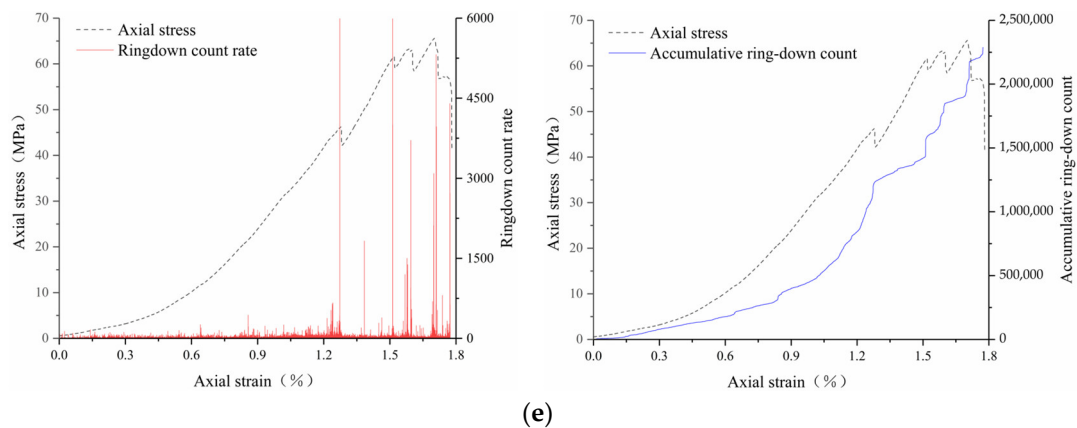


Figure 9. Cont.



**Figure 9.** The stress–strain curves of rock samples under different temperatures and corresponding change law of acoustic emission parameters. (a) 25 °C. (b) 500 °C. (c) 700 °C. (d) 900 °C. (e) 1100 °C.

Figure 9 illustrates that during the initial loading phase, the acoustic emission ringing count rate was not clear-cut, but it gradually increased in density as the loading advanced. The elevation of the temperature tended to result in a denser acoustic emission ringing count rate. This principle exists because acoustic emissions can be perceived as external outcomes stemming from the creation and development of internal cracks in rock samples, corresponding to the condition of the damage. The rock specimens experienced an increase in temperature, resulting in the formation and propagation of internal fissures, thereby augmenting the energy release rate and the ringing of acoustic emission.

Figure 9b–e illustrates the acoustic emission properties of rock specimens post-high-temperature processing. The results at temperatures of 900 °C and 1100 °C were significantly different from those at room temperature. At the outset of compaction, a rise in acoustic emission signals and a rapid rate of ringing were noticed, implying that high temperatures caused considerable thermal harm to the rocks, resulting in more distinct cracks than those in rocks exposed to ambient temperature. After the linear elastic stage was initiated, the ringing count rate stayed relatively low. After the linear elastic stage was entered, the ringing count rate was maintained at a relatively low level. After the stable crack-propagation stage was entered, the ringing count rate was improved to some extent, which can be distinguished from the linear elastic stage, but the activity of acoustic emission at high temperatures was not as intense as that at room temperature. After the unstable crack-propagation stage was entered, the ringing count rate suddenly rose to a small peak, but the increase was smaller than that at room temperature. Upon the stress attaining its maximum intensity, the rate of ringing did not hit this peak but was marginally delayed compared to the peak stress strength. At elevated temperatures, the initial harm to the rock specimens intensified, thus intensifying the acoustic emission signal during the initial loading stage. At high temperatures, the acoustic emission ringing count rate did not differ as drastically as at room temperature due to the increased ductility of rock, which causes the progressive failure process to be slower with a rise in strain than at room temperature.

## 5. Damage Evolution Law and Constitutive Model of Basalt

### 5.1. Damage Variable and Evolution Law of Basalt

The alteration in the cumulative ringing count is demonstrated to be linked to the alteration in mechanical properties and microstructure of materials [24]. Therefore, it is inferred that there is an inevitable connection between the total number of ringing and the progression of rock damage. The expression of damage variable  $D$  was derived from the normalized cumulative acoustic emission ringing count of Liu Baoxian et al. [25]:

$$D = Du \frac{Cd}{Co} = \left(1 - \frac{\sigma c}{\sigma p}\right) \frac{Cd}{Co} \quad (1)$$

The critical damage value,  $D_u$ , is represented by the residual strength,  $\sigma_c$ , and the peak strength,  $\sigma_p$ . The total count of acoustic emission ringing at each phase of the rock sample compression failure during the test,  $C_d$ , is represented by  $C_d$ , and the aggregate count of acoustic emission ringing throughout the compression failure of the rock sample,  $C_o$ , is also shown by  $C_o$ .

By employing Formula (1) as shown in Figure 10, one can deduce the axial stress–axial strain and the variable–axial strain curves for basalt under uniaxial compression at ambient temperature.

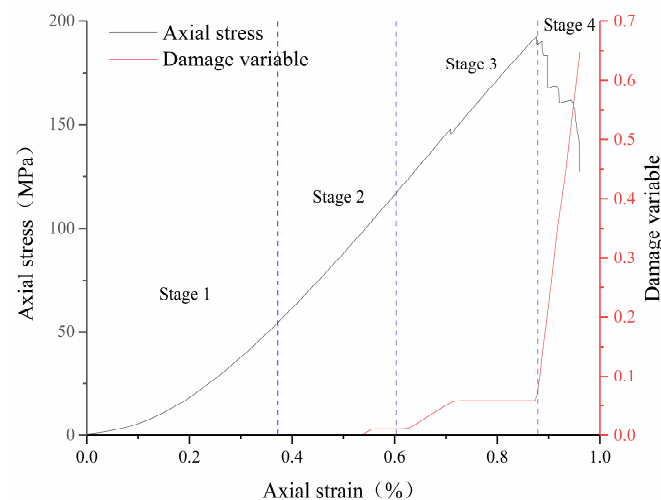


**Figure 10.** Axial stress–axial strain curve and damage variable–axial strain curve of basalt under uniaxial compression at room temperature.

The figure illustrates that the progression of damage in rock samples subjected to uniaxial compression is segmented into four distinct phases. At the start of harm, the damage factor's worth is negligible. The rock samples are in the crack-closure stage, with only a few cracks having been shut. The microcracks and fractures in the rock samples have not grown, and the acoustic emissions causing ringing are still insignificant. As the rock samples gradually deteriorate, the phase of harm development is in line with the elastic phase, and the phase of crack spread is consistent. As the original crack and the newly initiated ones expand, the acoustic emission ringing count rises in a steady manner. Figure 10 illustrates that the damage variable rises with a rise in strain. In the swift development stage of damage, the rock sample transitions into an unstable stage of crack expansion, where both the initial and newly developed cracks in the sample gradually expand, converge, and eventually appear as extensive cracks. Elastic strain energy emission escalates rapidly, evidenced by unusually vigorous acoustic emission and a marked rise in the damage variable, as depicted in Figure 10. During the stage of damage failure, rock specimens transition into residual deformation following the creation of large-scale cracks. The progression of the damage variable, aligning with the stress–strain curve's post-peak failure phase, aptly mirrors the entire gradual breakdown of internal cracks in the rock specimens, including compaction, initial development, stable propagation, unstable propagation, convergence, and connection until failure.

An analysis of basalt's axial strain patterns at different temperatures shows that after reaching high temperatures, the rock samples exhibited a notably elevated level of damage during the early loading stage, where elevated temperatures are linked to higher values in the initial phase. This suggests that a rise in temperature results in greater initial thermal damage to the rock and hastens the development of its internal fractures. As the temperature rises, the strain intensifies due to a considerable rise in the harm factor, thus slowing the rock samples' failure rate.

### 5.2. Constitutive Model Based on Acoustic Emission Parameters

Utilizing the concepts of continuous damage mechanics and Formula (1), the constitutive model of rock under uniaxial compression can be inferred as follows:

$$\sigma = (1 - D)E\varepsilon = \left[1 - \left(1 - \frac{\sigma_c}{\sigma_p}\right)\frac{C_d}{C_0}\right]E\varepsilon \quad (2)$$

Liu Baoxian et al. [25] discovered that, to a certain degree, the model can reflect the axial stress–axial strain relationship of rocks, where  $\varepsilon$  is the axial strain. However, the stress–strain curve of the model during the crack-closure stage is essentially a straight line, which is markedly distinct from the curve with a gradually rising gradient in the experiment. The acoustic emission signals generated during the rock's crack-closure phase are minuscule when compared to those generated in the gradual breakdown period. This results in the  $C_d/C_0$  ratio being very small and unchanged, such that  $1 - D$  is approximately constant. It can be seen from Formula (2) that the stress at this stage increases with the strain line, which is quite different from the test result curve. The theory of effective medium thus serves as the basis for the adoption of the negative exponential model in the crack-closure stage. After the crack-closure stage, the foundational model, grounded in acoustic emission parameters, has been adopted.

#### 5.2.1. Constitutive Model of Crack-Closure Stage

In 2015, Peng et al. [26] proposed a negative exponential model to comprehend axial strain and stress in fissures, a concept backed by substantial experimental data and universally acknowledged for its precise accuracy in fitting. Utilizing the effective medium theory, Peng et al. split the axial strain of the crack into two sections: the axial strain of the matrix and the axial strain of the crack. Further examination of the experimental data revealed that, with a rise in axial stress, the crack's axial strain gradually rises, and its growth rate gradually diminishes, eventually settling into a gentle state. Therefore, an established negative exponential model depicted the crack's axial strain correlating with alterations in axial stress. The effective medium theory serves as the basis for this research, which suggests that the relationship between axial strain and the axial stress of the crack follows a negative exponential pattern.

The axial strain  $\varepsilon^m$  of the matrix and the crack axial strain  $\varepsilon^c$  can be divided into two components of rock:

$$\varepsilon = \varepsilon^m + \varepsilon^c \quad (3)$$

Hooke's law dictates that the axial strain of the matrix is

$$\varepsilon^m = \frac{\sigma}{E} \quad (4)$$

The concentration of minuscule fractures within the rock is the chief factor impacting the axial stress of these cracks; if it is a consequence of axial stress, then there is

$$\varepsilon = \frac{\sigma}{E} + \varepsilon^c(\sigma) \quad (5)$$

By means of Formulas (3) and (4), it is feasible to ascertain the axial strain of cracks in rock specimens at different temperatures, and Figure 11 displays the association between this strain and the axial stress. It is deduced that with the intensification of axial stress, there is a gradual increase and eventual stabilization of axial strain in a crack, in line with the negative exponential model, which can be expressed as follows.

$$\varepsilon^c = a \left[1 - \exp\left(-\frac{\sigma}{b}\right)\right] \quad (6)$$

where  $a$  is the maximum crack closure amount, and  $b$  is the model parameter related to temperature.

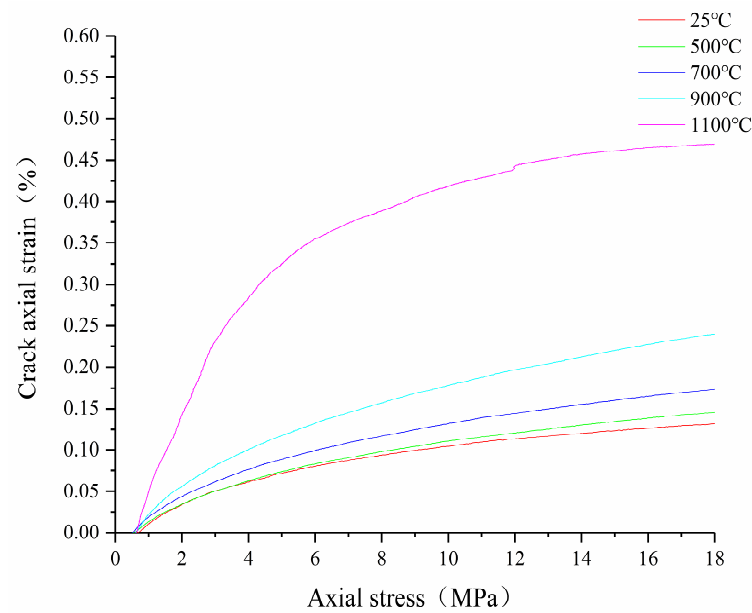


**Figure 11.** The relationship between crack axial strain and axial stress of basalt at different temperatures.

Formula (6) was employed to model the association between the axial strain and axial tension of fractures on rock samples at varying temperatures, thereby allowing for the determination of basalt's mechanical properties at these temperatures, as seen in Table 1. As temperatures rose, studies revealed a steady rise in the highest possible degree of crack sealing, implying a surge in the initial thermal harm to rock specimens, which is in agreement with the initial damage law variable  $D$  depicted in Figure 12.

**Table 1.** Mechanical parameters of basalt at different temperatures.

Temperature/°C	Peak Strength/MPa	Elastic Modulus/MPa	a/%	b/MPa	R <sup>2</sup>
25	192.56	271.98	0.164	9.889	0.99
500	185.04	213.94	0.203	13.35	0.99
700	170.54	212.21	0.254	14.81	0.98
900	127.63	145.16	0.364	15.73	0.99
1100	65.64	56.91	0.493	5.145	0.98

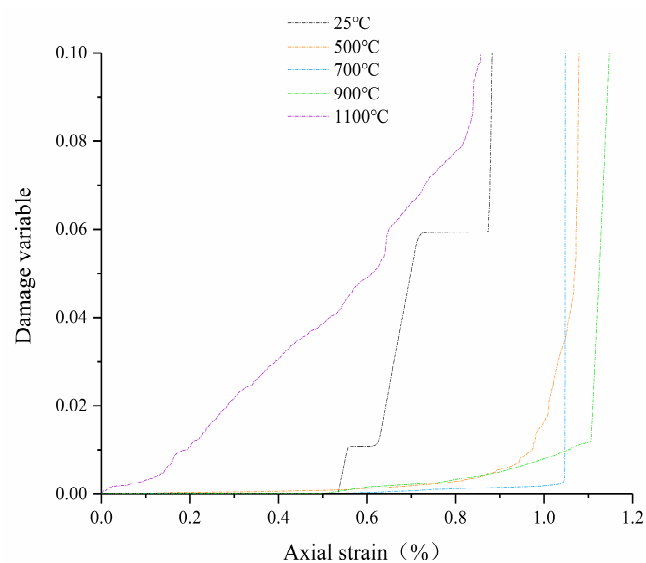


**Figure 12.** Basalt damage variable–axial strain curves at different temperatures.

Substituting Formula (6) into Formula (5) yields the following stress–strain correlation in the crack-closure stage:

$$\varepsilon = \frac{\sigma}{E} + a \left[ 1 - \exp\left(-\frac{\sigma}{b}\right) \right] \quad (7)$$

In Figure 13, a juxtaposition is presented between the model's theoretical trajectory and the experimental basalt curve at the crack-closure phase after various high-temperature treatments, with the model's findings aligning with those of the experiments.

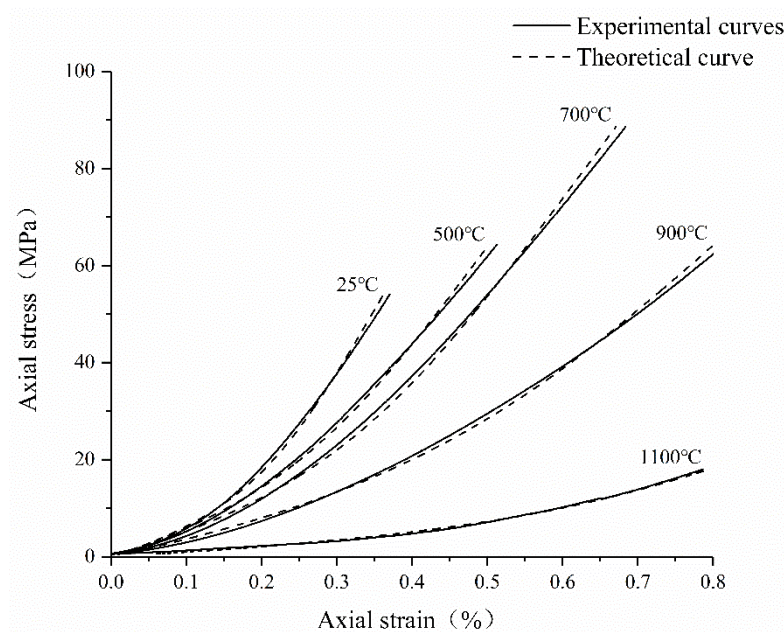


**Figure 13.** The comparison between the theoretical curve and the experimental curve of the model in the crack-closure stage.

### 5.2.2. Constitutive Model Based on Acoustic Emission Parameters after Crack Closure

The crack-closure stage saw a relatively small number of signals emitted acoustically by the rocks, as was previously noted in the analysis of basalt's acoustic emission characteristics. However, the elastic stage began to generate acoustic emission signals. A model that takes into account stress–strain through acoustic emission parameters was formulated, since the count of acoustic emission rings in the rock samples was determined by the strain experienced at the crack's closure, when the crack is completely shut.

At point D, the line connecting point B meets the strain axis, which is the strain at which the crack is completely shut, known as the crack-closure strain  $\varepsilon^c$ . Figure 14 illustrates the OB section as the crack-closure stage, the BC section as the elastic stage, and point C as the crack initiation stress. From this point, the cumulative ringing count is calculated, and Formula (2) is revised as follows.

$$\sigma = (1 - D)E(\varepsilon - \varepsilon^c) = \left[ 1 - \left( 1 - \frac{\sigma_c}{\sigma_p} \right) \frac{C'_d}{C'_0} \right] E(\varepsilon - \varepsilon^c) \quad (8)$$

where  $C'_d$  and  $C'_0$  are the cumulative acoustic emission ringing count in each stage of the rock sample compression failure process and the cumulative acoustic emission ringing count in the whole rock sample compression failure process calculated from point D, respectively.

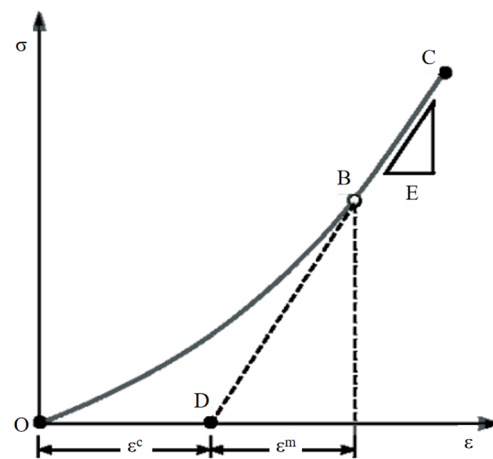


Figure 14. Crack closure strain diagram.

In Figure 15, a juxtaposition is presented between the model’s theoretical trajectory, derived from acoustic emission parameters, and the actual experimental trajectory following the sealing of rock samples at 500 °C. The figure illustrates that the model’s curve aligns closely with the experimental curve following the phase of crack closure.

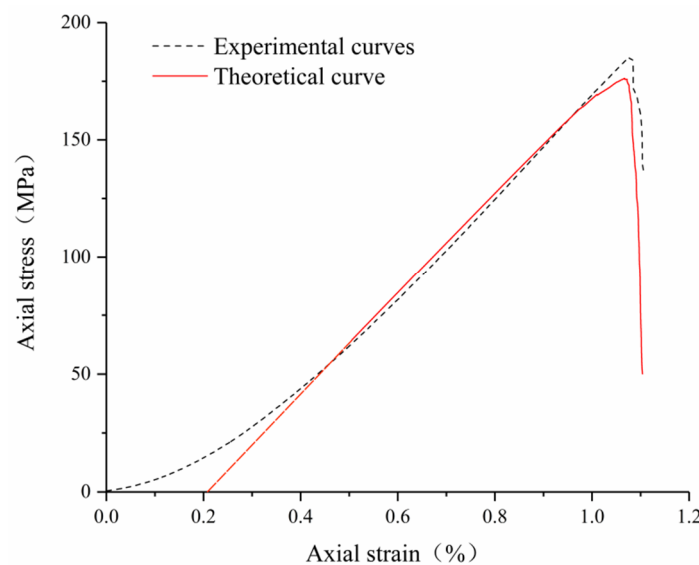


Figure 15. A comparison diagram of the theoretical curve and the experimental curve of the model based on the acoustic emission parameters after the crack closure of the rock sample at 500 °C.

### 5.2.3. Stress–Strain Constitutive Model of the Whole Process

By analyzing the preceding data, a stress–strain constitutive model for the entire rock failure process can be constructed, taking into account the crack-closure effect and acoustic emission parameters.

$$\begin{cases} \varepsilon = \frac{\sigma}{E} + a \left[ 1 - \exp\left(-\frac{\sigma}{b}\right) \right] & (\varepsilon < \varepsilon_0) \\ \sigma = \left[ 1 - \left( 1 - \frac{\sigma_c}{\sigma_p} \right) \frac{C'_d}{C'_0} \right] E(\varepsilon - \varepsilon^c) & (\varepsilon > \varepsilon_0) \end{cases} \quad (9)$$

where  $\varepsilon_0$  is taken as the critical strain point of the negative exponential model curve before crack closure and the constitutive model curve based on acoustic emission parameters after crack closure.

Figure 16 presents a juxtaposition of the theoretical and experimental trajectories regarding the axial stress–strain correlation in rock specimens exposed to varying elevated

temperatures. It can be seen that this model effectively mirrors the various phases in the gradual deterioration of rock, such as the compaction stage, elastic stage, stable crack-propagation stage, unstable crack-propagation stage, and failure stage.

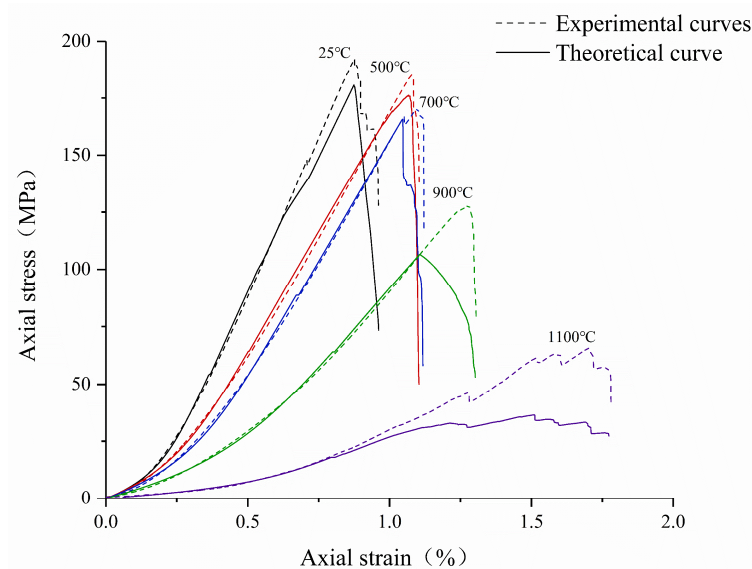


**Figure 16.** Comparison diagram of theoretical curve and experimental curve of thermal damage basalt.

#### 5.2.4. Discussion on Constitutive Model

In the case of rocks, varying temperatures lead to a decrease in stress upon reaching its maximum, accompanied by a notable increase in the number of acoustic emission rings. The acoustic emission ringing of the post-peak stage, which is only a small part of the total count produced during the rock-failure phase, diminishes and stays minimal as the frequency of ringing decreases. It is hard to accurately gauge the residual stress of brittle rocks when compressed without a single layer. Consequently, Figure 16 illustrates a notable divergence between the anticipated and actual data curves in the post-peak stage. As the temperature rises, the progressive breakdown of rock becomes slower, resulting in a lesser stress change value from the same strain increment. Consequently, acoustic emission equipment can be used to closely monitor the internal crack formation and convergence of rock samples. Nevertheless, the experimental value is flawed, as it is higher than the theoretical curve due to the end effect. Theoretically, the model's agreement with experimental results is strong, suggesting it is a major factor in the formation of thermal harm in basalt.

## 6. Conclusions

This study conducted a uniaxial compression test and acoustic emission monitoring of basalt at various temperatures. The mechanical, acoustic, damage evolution, and stress-strain models of its progressive failure process were then examined. The ensuing deductions were derived:

1. Examining the stress-strain relationship reveals that as the temperature rises, the trend of the curve becomes more gradual, with a broader range of change above 700 °C, and the highest strain exhibits a steady growth pattern, suggesting that elevated temperatures enhance the flexibility of basalt samples. The curve after 1100 °C has stress fluctuation, showing certain plastic characteristics.
2. Analyzing the peak frequency distribution of sound emissions during the loading stage shows that high temperatures significantly affect the expansion speed and size of cracks in the basalt-loading stage. Fissures caused by thermal damage shorten the time it takes for small cracks to form in the initial stage of rock samples, accelerating their expansion but limiting their total spread, providing a vital theoretical

basis for identifying initial indicators of rock fracture instability after exposure to high temperatures.

3. As the temperature reaches 1100 °C and the treatment temperature rises, the rock sample's mode of failure shifts from shear to tensile failure, accompanied by various crack types in the failure area. Variations in fracture patterns are linked to the presence of tensile and shear cracks. Simultaneously, a comparative study shows that the critical temperature for the phase change in basalt mineral lies between 700 °C and 900 °C.
4. Elevated temperatures lead to heat-induced harm to basalt, resulting in the rock specimens exhibiting active acoustic emissions during the early loading phase. Furthermore, as elevated temperatures enhance the rock's malleability, the gradual breakdown process slows down compared to room temperature due to heightened strain, and the acoustic emission factors, like the rate of ringing, remain relatively stable at room temperature.
5. There are four distinct phases in the development of damage in rock specimens under standard temperature scenarios. After high-temperature processing, rock samples initially suffer more thermal harm, and as the temperature increases, so does the initial thermal damage and the rate of damage development.
6. Utilizing the negative exponential model, grounded in effective medium theory and acoustic emission parameters, the strain point for crack closure was established. Following this, it was integrated with two theoretical models to create a comprehensive process constitutive model, encompassing the definition of acoustic emission parameters and considering the crack-closure phenomenon. Relative to the test curve, the model's overall accuracy is commendable, accurately representing every key mutation point on the stress–strain curve and proving useful for analyzing rock's failure under elevated temperatures.

**Author Contributions:** W.C.: formal analysis, investigation, visualization, and funding acquisition. R.C.: conceptualization, methodology, and supervision. X.L.: writing—review. Y.C.: writing—review. F.Z.: editing. D.L.: writing—review. Z.W.: editing. All authors have read and agreed to the published version of the manuscript.

**Funding:** The Hunan Postgraduate Research Innovation Project (No. QL20220216) was supported by the Hunan Provincial Natural Science Foundation of China (No. 2023JJ30511), the Research Foundation of the Department of Natural Resources of Hunan Provincial of China (No. 20230144DZ), the Educational Commission of the Hunan Province of China (Key Program) (No. 18A252), the National Natural Science Foundation of China (No. 42061011, No. 41977236), the Natural Science Foundation of the Jiangxi Province of China (No. 20223BBG71W01), and the Xinjiang Corps Science and Technology Program (No. 2020AB003).

**Institutional Review Board Statement:** Not applicable.

**Informed Consent Statement:** Not applicable.

**Data Availability Statement:** No new data were created or analyzed in this study. Data sharing is not applicable to this article.

**Acknowledgments:** The authors sincerely appreciate the support from the funds above.

**Conflicts of Interest:** The authors declare no conflicts of interest in this work. The authors declare that we have no financial or personal relationships with other people or organizations that can inappropriately influence our work, and there is no professional or other personal interest of any nature or kind in any product, service, and/or company that could be construed as influencing the position presented in, or the review of, the manuscript entitled, “Mechanical properties and damage constitutive model of thermally damaged basalt”.

## References

1. Xu, M.; Yi, Q.; Shan, Y.; Xiong, S.; Cao, H.; Yi, S. Collaborative quality-value modelling of nuclear power equipment intelligent manufacturing based on system power flow diagram. *J. Mech. Eng.* **2022**, *58*, 270–282.
2. Meng, Y.C.; Wu, H.S. World's nuclear power plants in 2021. *Foreign Nucl. News* **2022**, *21*, 26–31.

3. Zhang, Q.C.; Jiang, Y.S.; Zhao, X.; Zhang, Y.P.; Zhao, K.; Zhang, B.B.; Lu, D.Z.; Huang, Y.L. Research progress on the hazards of high-level nuclear waste radiation to the deep geological disposal environment and storage tank materials. *Equip. Environ. Eng.* **2022**, *19*, 86–93.
4. Qiao, J.; Wang, G.; Song, L.; Liu, X.; Zhou, C.; Niu, Y.; Liu, B. Mechanical properties and the mechanism of microscopic thermal damage of basalt subjected to high-temperature treatment. *Nat. Hazards.* **2024**, *120*, 41–61. [[CrossRef](#)]
5. Wong, L.N.Y.; Zhang, Y.; Wu, Z. Rock strengthening or weakening upon heating in the mild temperature range? *Eng. Geol.* **2020**, *272*, 105619. [[CrossRef](#)]
6. Wu, Y.; Li, X.-Z.; Huang, Z.; Wang, Y.-C.; Deng, L.-C. Effect of thermal damage on tensile strength and microstructure of granite: A case study of Beishan, China. *Geomech. Geophys. Geo Energy Geo Resour.* **2021**, *7*, 82. [[CrossRef](#)]
7. Wagner, H. Deep mining: A rock engineering challenge. *Rock Mech. Rock Eng.* **2019**, *52*, 1417–1446. [[CrossRef](#)]
8. Shen, Y.-J.; Hao, J.-S.; Hou, X.; Yuan, J.-Q.; Bai, Z.-P. Crack propagation in high-temperature granite after cooling shock: Experiment and numerical simulation. *Bull. Eng. Geol. Environ.* **2021**, *80*, 5831–5844. [[CrossRef](#)]
9. Zhao, X.G.; Xu, H.R.; Zhao, Z.; Guo, Z.; Cai, M.; Wang, J. Thermal conductivity of thermally damaged Beishan granite under uniaxial compression. *Int. J. Rock Mech. Min. Sci.* **2019**, *115*, 121–136. [[CrossRef](#)]
10. Tang, Z.C.; Sun, M.; Peng, J. Influence of high temperature duration on physical, thermal and mechanical properties of a fine-grained marble. *Appl. Therm. Eng.* **2019**, *156*, 34–50. [[CrossRef](#)]
11. Gautam, P.; Verma, A.; Jha, M.; Sharma, P.; Singh, T. Effect of high temperature on physical and mechanical properties of Jalore granite. *J. Appl. Geophys.* **2018**, *159*, 460–474. [[CrossRef](#)]
12. Yin, T.; Chen, Y.; Li, X.; Li, Q. Effect of high temperature and strain rate on the elastic modulus of rocks: A review. *Int. J. Earth Sci.* **2021**, *110*, 2639–2660. [[CrossRef](#)]
13. Zhu, Z.; Jiang, G.; Tian, H.; Dou, B. Research on statistical thermal damage constitutive model of rock based on Normal distribution. *J. Cent. South Univ.* **2019**, *50*, 1411–1418.
14. Liu, W.; Dan, Z.; Jia, Y.; Zhu, X. On the statistical damage constitutive model and damage evolution of hard rock at high-temperature. *Geotech. Geol. Eng.* **2020**, *38*, 4307–4318. [[CrossRef](#)]
15. Zhu, Y.; Yu, J.; Cai, Y.; Tang, X.; Yao, W.; Liu, X. A novel fatigue damage model of rock considering temperature effects. *Adv. Civ. Eng.* **2020**, *2020*, 8838335. [[CrossRef](#)]
16. Wang, F.; Konietzky, H. Thermo-mechanical properties of granite at elevated temperatures and numerical simulation of thermal cracking. *Rock Mech. Rock Eng.* **2019**, *52*, 3737–3755. [[CrossRef](#)]
17. Wang, S.; Liao, H.; Chen, Y.; Fernández-Steeger, T.M.; Du, X.; Xiong, M.; Liao, S. Damage evolution constitutive behavior of rock in thermo-mechanical coupling processes. *Materials* **2021**, *14*, 7840. [[CrossRef](#)] [[PubMed](#)]
18. Qin, Y.; Tian, H.; Xu, N.-X.; Chen, Y. Physical and mechanical properties of granite after high-temperature treatment. *Rock Mech. Rock Eng.* **2020**, *53*, 305–322. [[CrossRef](#)]
19. Takarli, M.; Prince, W.; Siddique, R. Damage in granite under heating/cooling cycles and water freeze–thaw condition. *Int. J. Rock Mech. Min. Sci.* **2008**, *45*, 1164–1175. [[CrossRef](#)]
20. Xu, X.L.; Zhang, Z.Z. Acoustic emission and damage characteristics of granite subjected to high temperature. *Adv. Mater. Sci. Eng.* **2018**, *2018*, 8149870. [[CrossRef](#)]
21. Altindag, R.; Güney, A. ISRM suggested method for determining the shore hardness value for rock. *Int. J. Rock Mech. Min. Sci.* **2006**, *43*, 19–22. [[CrossRef](#)]
22. Zhang, W.; Sun, Q.; Hao, S.; Geng, J.; Lv, C. Experimental study on the variation of physical and mechanical properties of rock after high temperature treatment. *Appl. Therm. Eng.* **2016**, *98*, 1297–1304. [[CrossRef](#)]
23. De Groot, P.J.; Wijnen, P.A.M.; Janssen, R.B.F. Real-time frequency determination of acoustic emission for different fracture mechanisms in carbon/epoxy composites. *Compos. Sci. Technol.* **1995**, *55*, 405–412. [[CrossRef](#)]
24. Ge, Z.; Sun, Q. Acoustic emission (AE) characteristics of granite after heating and cooling cycles. *Eng. Fract. Mech.* **2018**, *200*, 418–429. [[CrossRef](#)]
25. Liu, B.; Huang, J.; Wang, Z.; Liu, L. Study on damage evolution and acoustic emission characteristics of coal rock under uniaxial compression. *Chin. J. Rock Mech. Eng.* **2009**, *28*, 3234–3238.
26. Peng, J.; Rong, G.; Cai, M.; Zhou, C.-B. A model for characterizing crack closure effect of rocks. *Eng. Geol.* **2015**, *189*, 48–57. [[CrossRef](#)]

**Disclaimer/Publisher’s Note:** The statements, opinions and data contained in all publications are solely those of the individual author(s) and contributor(s) and not of MDPI and/or the editor(s). MDPI and/or the editor(s) disclaim responsibility for any injury to people or property resulting from any ideas, methods, instructions or products referred to in the content.